Ru–Ni nanoparticles electrodeposited on rGO/Ni foam as a binder-free, stable and high-performance anode catalyst for direct hydrazine fuel cell

Tahereh Mohammadi [a], Karim Asadpour-Zeynali [a,**], Mir Reza Majidi [b], Mir Ghasem Hosseini [b,c,*]

[a] Department of Analytical Chemistry, Faculty of Chemistry, University of Tabriz, Tabriz, Iran
[b] Electrochemistry Research Laboratory, Department of Physical Chemistry, Chemistry Faculty, University of Tabriz, Tabriz, Iran
[c] Engineering Faculty, Department of Materials Science and Nanotechnology, Near East University, 99138 Nicosia, North Cyprus, Mersin 10, Turkey

A B S T R A C T

Bimetallic Ru–Ni nanoparticles was synthesized on the reduced graphene oxide decorated Ni foam (Ru–Ni/rGO/NF) by electroplating method to be utilized as the anode electrocatalyst for direct hydrazine-hydrogen peroxide fuel cells (DHzHPFCs). The synthesized electrocatalysts were characterized by X-ray diffraction, Field emission scanning electron microscopy, Fourier transform infrared spectroscopy, and Raman spectroscopy. The electrochemical properties of catalysts towards hydrazine oxidation reaction in an alkaline medium were evaluated by cyclic voltammetry, chronoamperometry, and electrochemical impedance spectroscopy. In the case of $Ru_1–Ni_3/rGO/NF$ electrocatalyst, $Ru_1–Ni_3$ provided active sites due to low activation energy (22.24 kJ mol^{-1}) for hydrazine oxidation reaction and reduced graphene oxide facilitated charge transfer by increasing electroactive surface area (EASA = 677.5 cm^2) with the small charge transfer resistance (0.1 Ω cm^2). The CV curves showed that hydrazine oxidation on the synthesized electrocatalysts was a first-order reaction in low concentrations of N_2H_4 and the number of exchanged electrons was 3.0. In the single cell of the of direct hydrazine-hydrogen peroxide fuel cell, the maximum power density value of $Ru_1–Ni_3/rGO/NF$ electrocatalyst was 206 mW cm^{-2} and the open circuit voltage was 1.73 V at 55 °C. These results proved that the $Ru_1–Ni_3/rGO/NF$ is a promising candidate for using as the free-binder anode electrocatalyst in the future application of direct hydrazine-hydrogen peroxide fuel cells due to its excellent structural stability, ease of synthesis, low cost, and high catalytic performance.

1. Introduction

In recent years, attention has been paid to direct hydride fuel cells such as; sodium borne hydride ammonia and hydrazine [1–6]. The use of hydride fuels has solved some problems related to hydrogen fuel, such as difficult carriage, storage, and the safety of

hydrogen [7]. In addition, hydrazine is a fuel with high energy density, low material cost, and satisfactory stability at ambient conditions [8]. Unlike direct alcohol fuel cells, owing to the absence of carbon in hydrazine fuel, CO poisoning catalysts could not be a problem for the DHzFCs and it became causing the decrease in greenhouse gases. In addition, using of alkaline medium is another advantage of this fuel, which shows relatively lower corrosively than an acidic medium. The N_2H_4 oxidation (HzOR) with a four-electron reaction has explained by Equations (1)–(3). The theoretical cell voltage is 2.13 V, which is more than liquid and H_2–O_2 fuel cells [9].

$$Anode : N_2H_4 + 4OH^- \rightarrow N_2 + 4H_2O + 4e^- \quad E^0 = -1.21 \ V \ vs \ SHE \tag{1}$$

$$Cathode : 2H_2O_2 + 4H^+ + 4e^- \rightarrow 4H_2O \quad E^0 = 0.92 \ V \ vs \ SHE \tag{2}$$

$$Overall : N_2H_4 + 2H_2O_2 \rightarrow N_2 + 4H_2O \quad E^0 = 2.13 \ V \ vs \ SHE \tag{3}$$
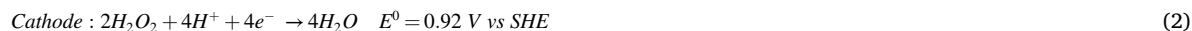
According to equation (3), HzOR products are nitrogen and water that both of them are compatible with the environment [10]. The only factor that limits the use of N_2H_4 in DHzHPFCs is its toxicity, which is fortunate according to Tanaka and coworkers, it can be solved with the formation of solid hydrazine by reacting hydrous hydrazine with carbonyl-containing polymer [11]. The preparation of a suitable catalyst is essential in the development of DHzHPFCs. For the HzOR, some non-noble and noble transition metals and their composite have been introduced as active catalysts [7,8]. Among the non-noble transition metals, Ni has a high catalytic activity for HzOR, but its permanence is relatively low and pure Ni is difficult to be used as a catalyst [12]. The natural activity of Ni can be increased by mixing other metals or non-metals to form compounds, for example, Ni-Pd [13], Ni-Zr [14], Ni-Fe [15], Ni-Co [16], Ni-Zn [17], Ni–S [18] and Ni–B [19], and Ni–P [8]. Usually, most of the catalysts are prepared by mixing catalysts powders and polymer binders to make membrane assembly electrode (MAE). Using polymer binders increases the electrode cost and as a result, catalyst will use fewer. On the other hand, due to the extended use of fuel cells, the catalyst materials are collapsed, which causes a decline in stability. Therefore, researches are concentrated on preparing the electrode, which uses a current collector such as Ni foam, Ti plate [20], and Cu foil [21]. Among these, Ni foam is a suitable substrate for anodic section, because Ni foam has excellent electrical conductivity and an open three-dimensional multichannel structure. Feng et al. has prepared Ni–Zn nanosheets on Ni foam and studied catalytic property for HzOR [22]. One of the innovations of this research is the use of the electrocatalyst in the anodic section without the ink of the electrocatalyst being immobilized on Nafion. This action causes the easy application of electrocatalyst on nickel foam, which has an accessible, stable and, relatively high efficiency compared to MEA.

In this research, Ru–Ni/rGO catalyst was prepared on Ni foam in two steps including electroreduction and electroplating. In the first step, the electrochemical reduction of graphene oxide (GO) to reduced graphene oxide (rGO) was carried out and in the second step, the Ru–Ni (1:3) bimetallic nanoparticles was electrodeposited on rGO/NF. Then, the characterization of Ru–Ni/rGO/NF catalyst was carried out by Field emission scanning electron microscopy (FE-SEM), X-ray diffraction (XRD), Fourier transform infrared spectroscopy (FT-IR) and Raman spectroscopy. The electrochemical behavior of electrocatalysts for HzOR in an alkaline solution was studied by cyclic voltammetry (CV), chronoamperometry (CA), and electrochemical impedance spectroscopy (EIS). Finally, an attempt was made to make a fuel cell with hydrazine fuel without immobilization catalytic inks on the Nafion; that means making a free-binder anode.

2. Experimental

2.1. Synthesis of catalyst

The Ni foam (NF, Ni > 99%, Latech, thickness 1.5 mm, Volumetric porosity (90–98%), Volumetric density (0.15–0.45 g cm^{-3}), Pores Per Inch (5–120 PPI) and porous structure) $1 \times 1 \times 0.15$ cm^3 was purified by sonicating in acetone for 30 min, followed by immersing in a 6.0 M HCl solution to eliminate surface oxide for 20 min. Then, the NF electrode was immersed in a solution of 4 gL^{-1} graphene oxide (GO) for 30 min. To stabilize the GO on the NF, it was placed in an oven at 60 °C for 2 h. After that, in a three-electrode cell, stabilized GO on NF was reduced in potassium hydrogen phthalate (40 gL^{-1}) solution at a potential of −1 V (vs. Ag/AgCl) for 1 h. In the last stage, Ru–Ni was electrodeposited on rGO/NF surface in a two-electrode cell from the electrolyte containing ruthenium chloride (RuCl$_3$.3H$_2$O, Merck) 5 gL^{-1}, ammonium chloride (NH$_4$Cl, 99.5% Merck) 50 gL^{-1}, nickel sulfamate (Ni (SO$_3$NH$_2$)$_2$.4H$_2$O, Merck) 6.45 gL^{-1}. The electrolyte temperature was 323 K with a deposition current 100 mA cm^{-2} for 30 min. For comparison, three electrodes were prepared by changing the ratio of RuCl$_3$.3H$_2$O to Ni (SO$_3$NH$_2$)$_2$.4H$_2$O in the electroplating solution (Ru: Ni, 1:3, 1:1, 3:1).

2.2. Characterization of catalysts

To characterize the surface morphology of the Ru–Ni/rGO/NF electrode, the field emission scanning electron microscopy equipped with an EDX micro analyzer (FE-SEM, TESCAN MIRA 3) was used. In addition, by X-ray diffraction pattern (XRD, Philips-PW 1730) with Cu Kα radiation in the 2θ range of 10–80°, the crystal structure of the catalyst was characterized. Besides, Fourier Transform infrared spectroscopy (FT-IR, PerkinElmer) and Raman spectroscopy (Teksan, Takram P50COR10 Spectrophotometer, 500-4000 cm^{-1} with 532 nm excitation source) were used to study the surface species of the synthesized Ru–Ni/rGO/NF electrode.

2.3. Electrochemical measurements of half-cell

The electrochemical tests were carried out in a three-electrode cell (one compartment) connected to an Origalys device (OrigaFlex-OGF01A/Potentiostat/Galvanostat, France). The Hg/HgO (MOE = mercury/mercury oxide) and platinum gauze (20 cm^2) immersed in 1.0 M NaOH solution were applied as the reference and counter electrodes, respectively, and the NF, rGO/NF, Ru–Ni/NF and Ru–Ni/rGO/NF were used as the working electrodes. Cyclic voltammetry (CV) and chronoamperometry (CA) experiments were performed to study the activity, stability, and electrochemical active surface area (EASA) of the synthesized electrocatalysts for hydrazine oxidation reaction (HzOR). To measure the electrical resistance of the synthesized electrocatalysts, the EIS technique was used in a frequency range of 10^5–10^{-1} Hz and the modulation potential of ± 10 mV.

3.1. Single - cell performance evaluation

The cell performance was investigated with a homemade fuel cell [23]. In this cell, the immobilized Pt/C (0.5 mg cm^{-2}) ink on Nafion 117 and the Ru$_1$–Ni$_3$/rGO on NF were used as cathode and anode, respectively. The prepared MEA was put in the fuel cell set-up and it was activated by the flow of water from each electrode and NaOH 2 M solution from the anode to convert H$^+$ of the Nafion membrane to Na$^+$ for 5 h. Finally, using the fuel cell set-up with feeding fuel (N$_2$H$_4$) from the anode and oxidant (H$_2$O$_2$) from the cathode, current density-voltage (I–V) and current density-power density (I–P) curves were extracted.
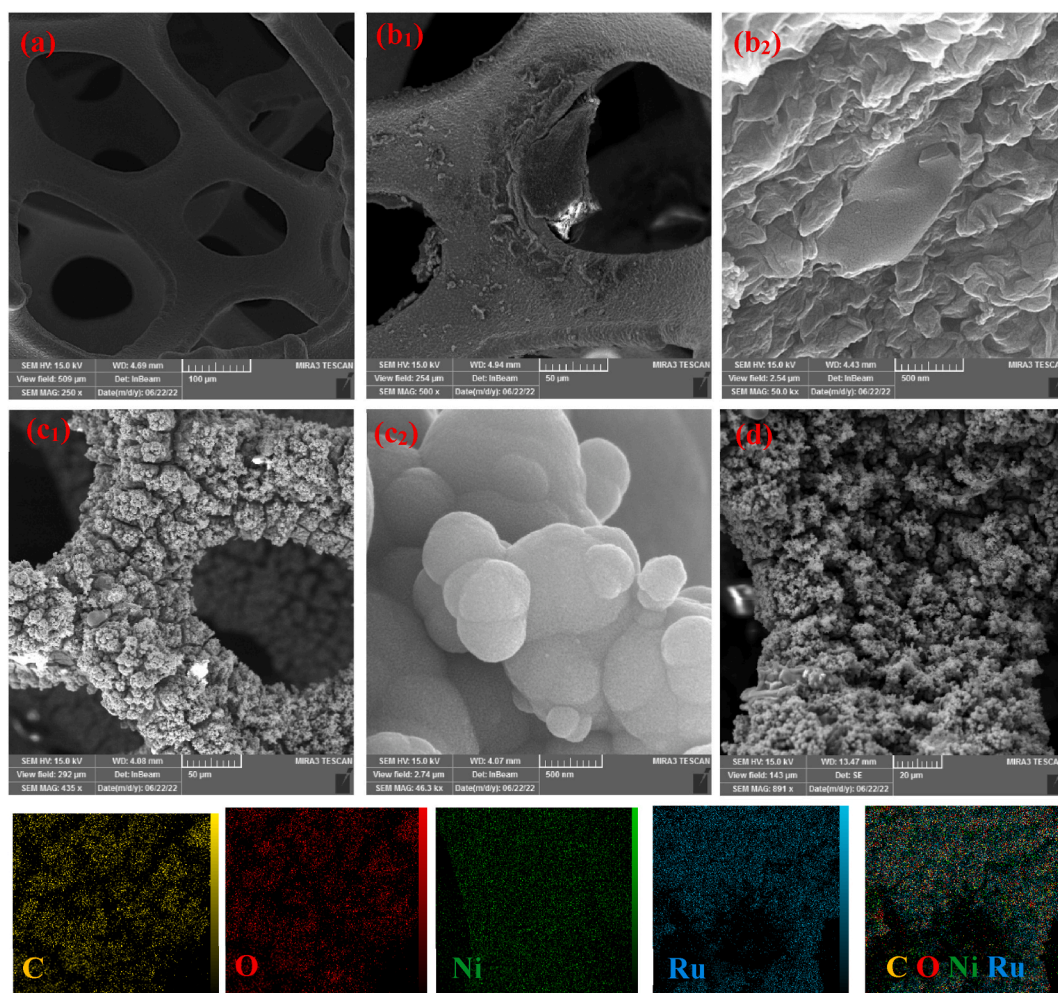

Fig. 1. FE-SEM images of (a) NF, (b$_1$, b$_2$) rGO/NF, (c$_1$, c$_2$) Ru$_1$–Ni$_3$/rGO/NF, (d) EDS mapping of C, O, Ni, Ru.

3. Results and discussion

3.1. The structural characterization of Ru–Ni/rGO/NF electrocatalyst

The surface morphologies of NF, rGO/NF, and Ru–Ni/rGO/NF electrocatalysts were demonstrated in Fig. 1. The commercial NF has the uniform and smooth surface with a unique 3D network structure that allows the deposition of the Ru–Ni/rGO electrocatalyst (Fig. 1a). After being immersed in the graphene suspension solution, the graphene sheets closely cover the skeleton of NF, indicating a good contact between graphene and NF (Fig. 1(b$_1$, b$_2$)). Interestingly, the rGO/NF maintains a special porous structure similar to bare NF, which is useful for electrolyte diffusion during the reaction. The FE-SEM images of the Ru$_1$–Ni$_3$/rGO/NF electrocatalyst is shown in Fig. 1 (c$_1$, c$_2$). The Ru–Ni alloy was uniformly and compactly aligned on the surface of rGO/NF. The morphology of Ru$_1$–Ni$_3$/rGO/NF electrocatalyst shows a rough surface covered by a spherical structure, which increases its specific surface area. In addition, this spherical structure increases the number of defects and active sites on the surface of the electrocatalyst, thereby improving the electrocatalytic reactivity [24,25]. Energy dispersive X-ray (EDX) spectrograms were recorded to characterize the distribution of the chemical element in the electrode surface. The FE-SEM and corresponding EDX mapping analysis of the Ru$_1$–Ni$_3$/rGO/NF electrode was shown in Fig. 1d. According to Fig. 1d, the elements of C, O, Ni, and Ru are uniform and dense on the whole surface of the Ru$_1$–Ni$_3$/rGO/NF electrode, this subject confirms that graphene, Ru and Ni homogeneously electrodeposited on the NF. It should be noted that, the presence of oxygen element on the electrode surface is due to incomplete electrochemical reduction of graphene oxide (GO). In addition, the presence of oxygen increases the hydrophobicity of graphene, which causes contact between the electrolyte and electrode [26,27].

The XRD patterns for NF, GO/NF, rGO/NF, and Ru$_1$–Ni$_3$/rGO/NF were shown in Fig. 2. For all four electrodes, the diffraction peaks at 2θ values of 44.54°, 51.9°, and 76.42° were related to the (111), (200), and (220) crystal planes of Ni (JCPDS Card NO.04-0850), respectively [28,29]. The intensity of Ru$_1$–Ni$_3$/rGO/NF was decreased compared with commercial NF. This result shows that Ru and Ni elementary materials were loaded on rGO/NF skeleton by an easy electroplating method. The XRD pattern does not display clear peaks for the Ru–Ni alloy, because the Ru–Ni deposited on the rGO/NF existed in amorphous phases [25]. In addition, the diffraction peaks of.

GO and rGO didn't appear in the XRD patterns of GO/NF, rGO/NF, and Ru–Ni/rGO/NF electrodes due to the strong Ni peaks [24].

The FT-IR spectra for GO/NF, rGO/NF, and Ru$_1$–Ni$_3$/rGO/NF electrodes are displayed in Fig. 3. Absorption bands shown in 2020, 1980, and 1920 cm^{-1} on these electrodes are related to the bending vibrations of the C–H group in aromatic compounds. Absorption bands are seen at 1640, and 1010 cm^{-1} on these electrodes are related to the stretching vibrations of C=C and C–O bonds respectively. Also in 1540 cm^{-1} a strong absorption band was seen that is related to the stretching vibration of the N–O group. In addition, the observation of absorption bands at 1700 and 1230 cm^{-1} seen only in the GO sample can be assigned to the carbonyl C=O and epoxy, indicating the abundance of oxygen containing-groups in the GO structure [30]. In addition, the decrease or even disappearance of oxygen-containing functional groups in rGO/NF and Ru$_1$–Ni$_3$/rGO/NF structure indicates that GO has been reduced successfully. Moreover, the presence of absorption bands at 619 and 671 cm^{-1} in the Ru$_1$–Ni$_3$/rGO/NF electrode is related to the stretching vibration of the Ni–O–H and Ni–O bond, respectively. This result proves the presence of nickel oxides and hydroxides in the electrode.

By Raman spectroscopy, the chemical features of GO and rGO samples were analyzed. To check whether the graphene oxide is completely reduced or not, Raman spectroscopy was used. According to Fig. 4, peaks around 1348 and 1595 cm^{-1} are related to the irregular vibration peak and regular graphite crystallite vibration of graphene, respectively. Before electroreduction, the intensity ratio of I$_D$/I$_G$ of GO sample is 0.96. After the reduction process, the ratio of I$_D$/I$_G$ of rGO rises to 1.1. The enhancement of the intensity ratio I$_D$/I$_G$ proves the successful reduction of GO again [31,32].
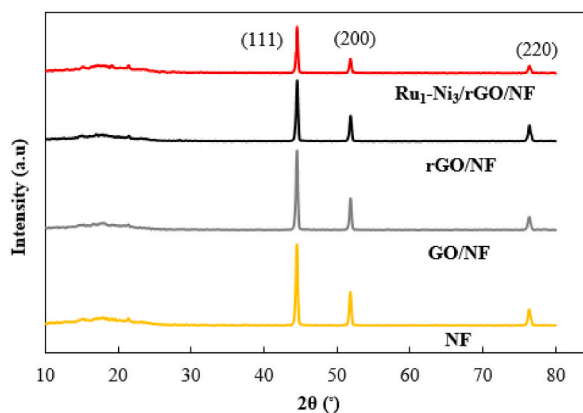

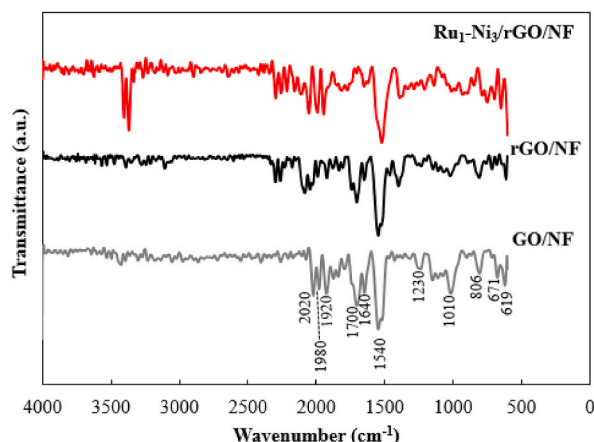**Fig. 2.** XRD patterns of NF, GO/NF, rGO/NF, and Ru$_1$–Ni$_3$/rGO/NF.

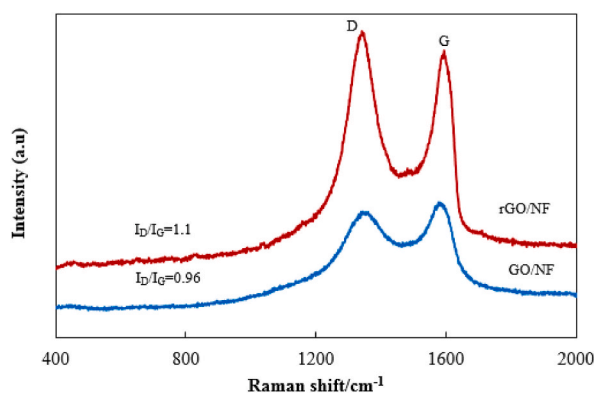**Fig. 3.** FT-IR spectra of GO/NF, rGO/NF, and Ru$_1$–Ni$_3$/rGO/NF.

Fig. 4. Raman spectra of GO/NF and rGO/NF.

3.2. Optimization of the catalyst and its electrochemical measurements

By adsorbing ions or molecules on the electrode surface, the electrocatalytic reaction mainly, happens. Therefore, a key factor for electrode performance is the electrochemical active surface area (EASA). The value of electrode double layer capacitance (C$_d$) is helpful in obtaining the nano-materials electrode's surface area [33]. CVs of NF, rGO/NF, Ru$_1$–Ni$_3$/NF, Ru$_1$–Ni$_3$/rGO/NF, Ru$_1$–Ni$_1$/rGO/NF, and Ru$_3$–Ni$_1$/rGO/NF electrodes were carried out at a non-Faraday zone of −0.1 to 0 V vs MOE in 1 M NaOH (Fig. 5a). Absorption and desorption of ions happened on the electrode surface in this potential region, and no electron transfer at the interface of the electrode. The electrode double layer capacitance (C$_d$) can be calculated from Eq. (4) [34,35].

$$di = C_d * d\upsilon \tag{4}$$

$$EASA = C_d / C^* \tag{5}$$

The relevance of scan rate and current density at −0.05 V vs MOE are shown in Fig. 5b. The electrode double layer capacitance (C$_d$) for six electrodes are demonstrated in Fig. 5b. According to Louie and Yeo's research [36,37], the specific theoretical double layer capacitance in alkaline solution (C*) of the Ni electrode is 40 μF cm^{-2} [38,39]. So, the EASA of electrodes can be obtained by Eq. (5). Although, it should be noted that correspondent of S. Trasatti's opinion, the capacitance value depends on changes in NaOH concentration, potential window, and other parameters. The electrode double layer capacitance (C$_d$) calculate by this method is a comparative value [34]. The results reveal that the Ru$_1$–Ni$_3$/rGO/NF electrode embraces the highest EASA. Therefore, the electrode of Ru$_1$–Ni$_3$/rGO/NF was selected as suitable electrode. The EASA of the Ru$_1$–Ni$_3$/NF electrode is 392.5 cm^2, while the EASA of the Ru$_1$–Ni$_3$/rGO/NF electrode is 677.5 cm^2. Results illustrate that the EASA of the Ru$_1$–Ni$_3$/rGO/NF electrode is approximately 1.7 times larger than Ru$_1$–Ni$_3$/NF electrode (Fig. 5c). These results powerfully indicate that rGO can be introduced as a good and compelling candidate for increasing the specific surface area of the Ru$_1$–Ni$_3$/rGO/NF electrode. Besides, the rGO deposited on the surface of NF not only kept the three-dimensional structure of NF but also provided defect sites for the growth of Ru and Ni nanoparticles [40].

To study the efficacy of rGO on the performance of the electrode, CV tests were carried out in 1 M NaOH and 0.06 M N$_2$H$_4$ for NF,
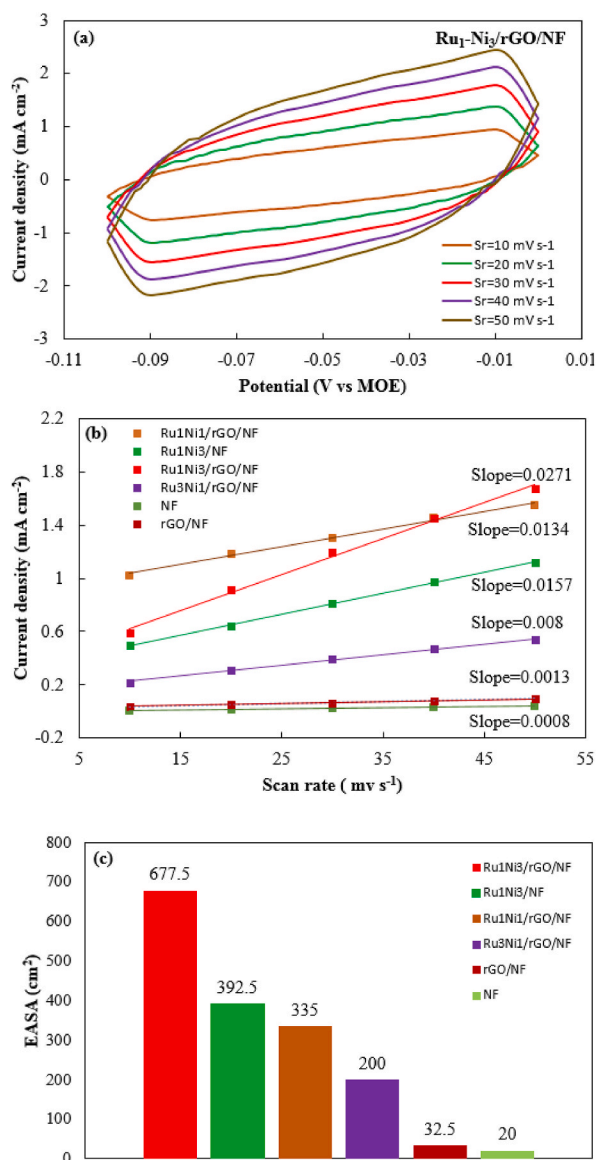
Fig. 5. (a) CV curves of Ru$_1$–Ni$_3$/rGO/NF catalyst under different scan rates (b) Plots of the averaged anodic current density at −0.05 V vs. MOE against scan rates of Ru$_1$–Ni$_3$/rGO/NF catalyst in 1 M NaOH (c) and Chart of EASA for different electrocatalysts.

rGO/NF, Ru$_1$–Ni$_3$/NF, and Ru$_1$–Ni$_3$/rGO/NF electrodes (Fig. 6). The results show that NF and rGO/NF have the lowest catalytic activity. In contrast, the Ru$_1$–Ni$_3$/NF and Ru$_1$–Ni$_3$/rGO/NF electrodes showed 28 mA cm^{-2} and 34 mA cm^{-2} (at −0.4 V), respectively. Actually, in the Ru$_1$–Ni$_3$/rGO/NF electrocatalyst, due to the presence of rGO, there are many places for the active substance of the Ru–Ni catalyst to sit. The results of electrochemical studies show that the current density of hydrazine electrooxidation and EASA for Ru$_1$–Ni$_3$/RGO/NF (677.5) catalyst is higher than Ru$_1$–Ni$_3$/NF (392.5), which is due to the different morphology of the catalysts. In the case of rGO, a large surface is provided for Ru$_1$–Ni$_3$/RGO/NF to sit, compared to the case of Ru$_1$–Ni$_3$/NF on nickel foam. These results strongly suggest that the introducing of rGO is an effective method to greatly increase the specific surface area of the electrode. In this regards similar explain is reported in the literature [40].

Fig. 7 presents the CV of Ru$_1$–Ni$_3$/rGO/NF electrode in the absence of N$_2$H$_4$ and in NaOH 1.0 M solution at the scan rate of 20 mV s^{-1}. In Fig. 7, an anodic peak and a cathodic peak can be observed. In an alkaline solution, at the potential window of 0.1–0.6 V and in anodic and cathodic scans, the pairs of Ni^{2+}/Ni^{3+} in the region (a$_1$) and (c) are converted to each other [41]. In addition, CV curve of the synthesized electrocatalyst in the presence of 0.1 M N$_2$H$_4$ in NaOH 1 M solution, the scan rate of 20 mV s^{-1} and the potential window of −1.2 to 0.8 V (vs. MOE) is displayed in Fig. 7. Peak (a$_2$) is related to hydrazine oxidation on the Ru$_1$–Ni$_3$/rGO/NF electrode according to Eq. (6):
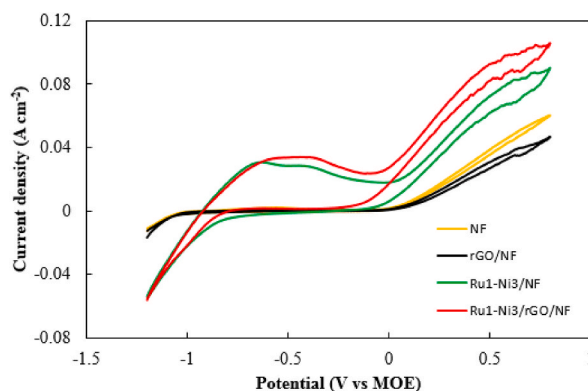
$$N_2H_4 + 4OH^- \rightarrow N_2 + 4H_2O + 4e^- \tag{6}$$

Fig. 6. CV curves of NF, rGO/NF, Ru_1–Ni_3/NF, and Ru_1–Ni_3/rGO/NF in NaOH 1 M + N_2H_4 0.06 M at the scan rate of 20 mV s^{-1}.
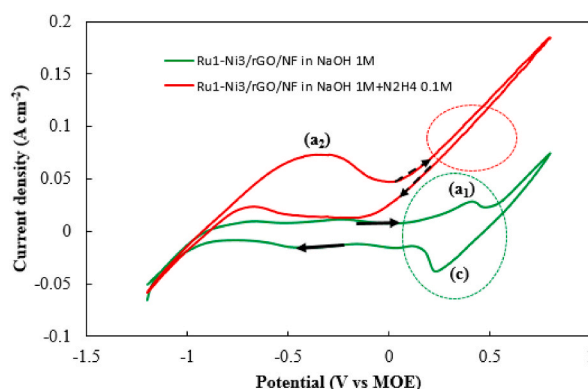

Fig. 7. CV curve of Ru_1–Ni_3/rGO/NF in NaOH 1 M and NaOH 1 M + N_2H_4 0.1 M at the scan rate of 20 mV s^{-1}.

The concentration of N_2H_4 was optimized during the HzOR on the Ru_1–Ni_3/rGO/NF electrocatalyst. The CV curves in a solution of NaOH 1.0 mol L^{-1} and varied concentrations of N_2H_4 at a sweep rate of 20 mV s^{-1} were recorded (Fig. 8a). By increasing N_2H_4 concentration, the HzOR peak potential is varied slightly towards positive values. The highest I_p value is obtained at N_2H_4 0.1 mol L^{-1}. This result proves the entity of a considerable number of electroactive species in solution. By plotting Log I_p values in terms of LogC, a straight linear relationship is obtained (Fig. 8b). The order of the HzOR on the Ru_1–Ni_3/rGO/NF electrocatalyst is gained from the slope of the Log I_p vs. Log C plot (Fig. 8b) according to Eqs. (7) and (8):

$$Rate = I_p = KC^n \tag{7}$$

$$Log\, I_p = Log k + n\, Log C \tag{8}$$

Where **k, C,** and **n** are the reaction rate constant and the bulk concentration of N_2H_4, and reaction order, respectively. The value of 0.90 is obtained for the Ru_1–Ni_3/rGO/NF electrocatalyst, which is close to value 1. This result shows that the HzOR with this electrocatalyst is of the first-order type and is in agreement with the values obtained in other works. The closer the value of the reaction order is to one, it shows that less hydrolysis reaction has occurred. Also, the linear relationship between current density and concentration shows that an irreversible electrochemical reaction has occurred on the electrode surface [42]. The CV curves recorded in 1 M NaOH and 0.04 M N_2H_4 at different scan rates (0.02–1.0 V s^{-1}) are shown in Fig. 9a. A linear relevance between the peak potential (Ep) and the scan rate can be seen in Fig. 9b, which indicates that this electrochemical process is irreversible. This subject has been described by Eq. (9) [43].

$$E_p = E^0 + \left[\frac{RT}{(1-\alpha)nF} \right] \left\{ 0.78 + ln\frac{D_0}{k_s} + ln\left[\frac{(1-\alpha)nF\nu}{RT} \right]^{\frac{1}{2}} \right\} \tag{9}$$

Where **E^0, R, T, α, n, F, D$_0$, k$_s$,** are the formal potential (V), the universal gas constant (8.314 J K^{-1} mol^{-1}), the temperature (K), the charge transfer coefficient, the number of electrons involved in the rate-determining step, the Faraday constant (96485 C mol^{-1}), the diffusion coefficient of N_2H_4 (cm^2 s^{-1}) and the standard heterogeneous rate constant (cm s^{-1}) respectively. According to Eq. (8), the slope of the curve in Fig. 9b was used to obtain the anodic charge transfer coefficient (α) in HzOR. The value of α was found 0.95 for the Ru_1–Ni_3/rGO/NF. Besides, by the Randles-Sevcik equation (Eq. (10)), the exchanged electrons number (n) in the HzOR reaction was
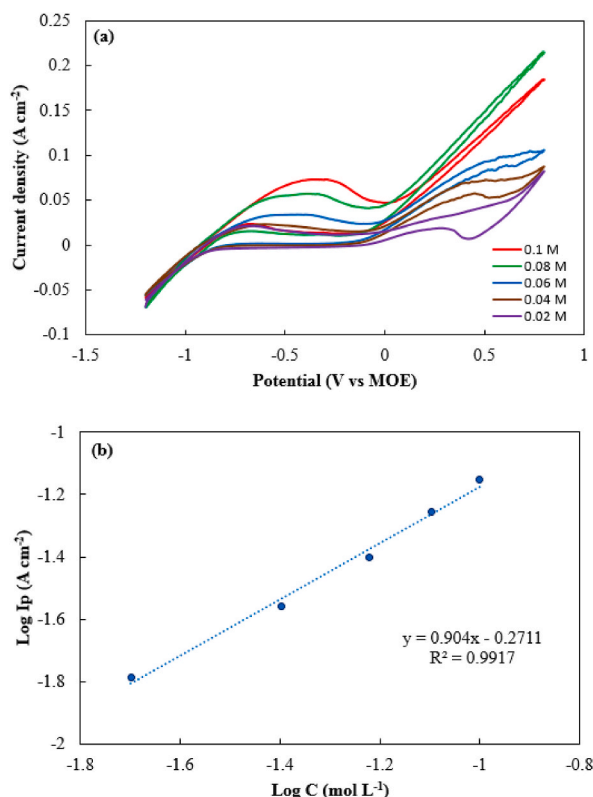
Fig. 8. (a) CV curves of Ru_1–Ni_3/rGO/NF for different concentrations of N_2H_4, (b) the relation of Log I_p vs. Log C $_{N2H4}$.

calculated [44].

$$i_p = 2.99 \times 10^5 n[(1-\alpha)n]^{\frac{1}{2}} A \, D_0^{1/2} \nu^{1/2} C_0^* \tag{10}$$

Where $\mathbf{i_p}$, $\mathbf{n}$, $\boldsymbol{\alpha}$, $\mathbf{A}$, $\mathbf{C_0^*}$, $\boldsymbol{\nu}$ and $\mathbf{D_0}$ are the peak current density (A cm^{-2}), the number of electrons involved in the rate-determining step, the anodic charge transfer coefficient, surface area (cm^2), N_2H_4 concentration (molcm^{-3}), the scan rate (Vs^{-1}), and the diffusion coefficient of N_2H_4 respectively. The diffusion coefficient (D_0) is considered to 5×10^{-5} cm^2 s^{-1} in 1.0 M NaOH solution [1]. Based on the obtained slope in Fig. 9(c), the n obtains 3.0 on the Ru_1–Ni_3/rGO/NF electrocatalyst. It shows that most of the oxidation reaction has occurred and the oxidation reaction dominates the hydrolysis.

Electrolyte temperature influence the performance of electrodes by affecting the rate of the charge transfer process at the electrode/electrolyte interface and mass diffusion in electrolyte solutions. Fig. 10a shows the CV curves of the Ru_1–Ni_3/rGO/NF at various temperatures in an aqueous solution of 1.0 M NaOH +0.04 M N_2H_4. The similar shapes of CV curves indicate the same mechanism at the examined temperatures. The peak oxidation current density of N_2H_4 on the Ru_1–Ni_3/rGO/NF electrocatalyst increases by increasing the temperature from 298 to 328 K. This is because of the endothermic reaction that is carried out on the Ru_1–Ni_3/rGO/NF electrode surface. By the Arrhenius equation (Eq. (11)), the activation energy (E_a, KJ mol^{-1}) was determined [45]:

$$-\frac{E_a}{RT^2} = \frac{\partial (Ln \, I_p)}{\partial T} \tag{11}$$

Where T, R, I_p, and E_a, are temperature (K), the gas constant (8.314 kJ mol^{-1}), the peak current density (A cm^{-2}), and activation energy (kJ mol^{-1}), respectively. Arrhenius plot of the Ru_1–Ni_3/rGO/NF electrocatalyst plotted in Fig. 10b. The E_a is determined from the slope of the curve. The E_a value for this electrocatalyst gained 22.24 kJ mol^{-1}. The low value of E_a for the Ru_1–Ni_3/rGO/NF electrocatalyst shows that the HzOR performed suitably on this electrocatalyst, which can attribute to the large specific surface area and enormous catalytic active sites through the unique frame of rGO/NF.

Fig. 11 shows the chronoamperometry response of Ru_1–Ni_3/rGO/NF and Ru_1–Ni_3/NF electrocatalysts in 0.04 M N_2H_4 + 1.0 M NaOH solution at −0.6 V (vs. MOE). According to Fig. 11, a sharp decline in the current density was observed at the initial seconds, and then the current density reached a pseudo steady-state at the initial seconds. Then, a few decreases in the current density was observed in each two electrocatalysts for longer times. From the comparison of these results, the Ru_1–Ni_3/rGO/NF electrocatalyst has better durability compared to Ru_1–Ni_3/NF in HzOR. In addition, the current density for the Ru_1–Ni_3/rGO/NF (0.023 A cm^{-2}) was demonstrated to be higher than the Ru_1–Ni_3/NF (0.004 A cm^{-2}) electrocatalyst, suggesting that the Ru_1–Ni_3/rGO/NF has higher catalytic
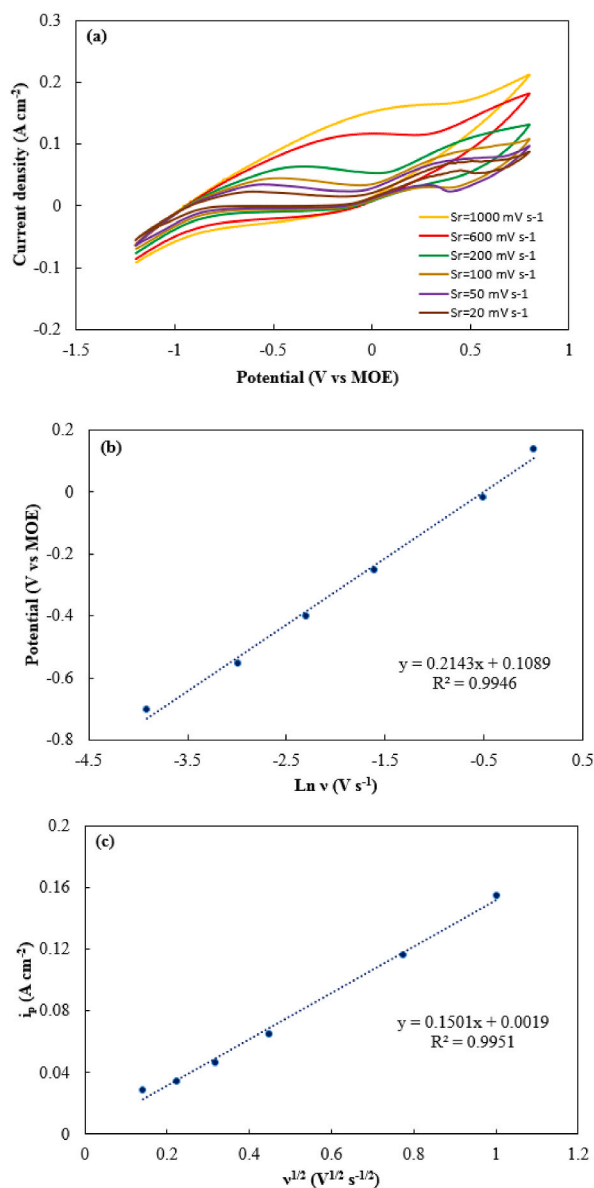
Fig. 9. (a) CV curves of Ru$_1$–Ni$_3$/rGO/NF for different scan rates in NaOH 1 M + N$_2$H$_4$ 0.04 M, (b) relation of E$_p$ vs. Ln ν, (c) relation of i$_p$ vs. $\nu^{1/2}$.

activity for HzOR than the Ru$_1$–Ni$_3$/NF of electrocatalyst. This result is in concord with the CV results.

The behavior of different anodic electrocatalysts (Ru$_1$–Ni$_3$/rGO/NF and Ru$_1$–Ni$_3$/NF) for hydrazine oxidation was studied using electrochemical impedance spectroscopy (EIS). EIS tests were performed in a solution of 1.0 M NaOH +0.1 M N$_2$H$_4$ at a potential of −0.25 V (vs. MOE). In the EIS spectrum, the observed semicircle corresponds to the electrochemical reactions on the surface of the electrocatalysts. The EIS information fitted according to the circuit proposed in Fig. 12 (a,b), where R$_s$, R$_{ct}$, CPE1, and W1 are solution resistance, charge transfer resistance, the constant phase element of the electrical double layer, and the Warburg element, respectively. In the high-frequency and low-frequency regions, the intersection of the horizontal axe with semicircles was used to estimate R$_s$ and R$_{ct}$, respectively. The quantity of R$_s$ and R$_{ct}$ is given in Table 1. According to Tables 1 and it can be seen that the rGO is improved the conductivity of Ru$_1$–Ni$_3$/rGO/NF with respect to the Ru$_1$–Ni$_3$/NF. So, the rGO has enhanced electrocatalytic properties due to its high electrical conductivity and structure with a large specific surface area. CV, CA, and EIS results are in good concord with each other and it can be inferred that the Ru$_1$–Ni$_3$/rGO/NF is better for usage in DHzHPFCs than other electrocatalysts.

3.3. Single fuel cell studies

In this part, the performance of the Ru$_1$–Ni$_3$/rGO/NF as the anode and Pt/C as the cathode in direct hydrazine-hydrogen peroxide
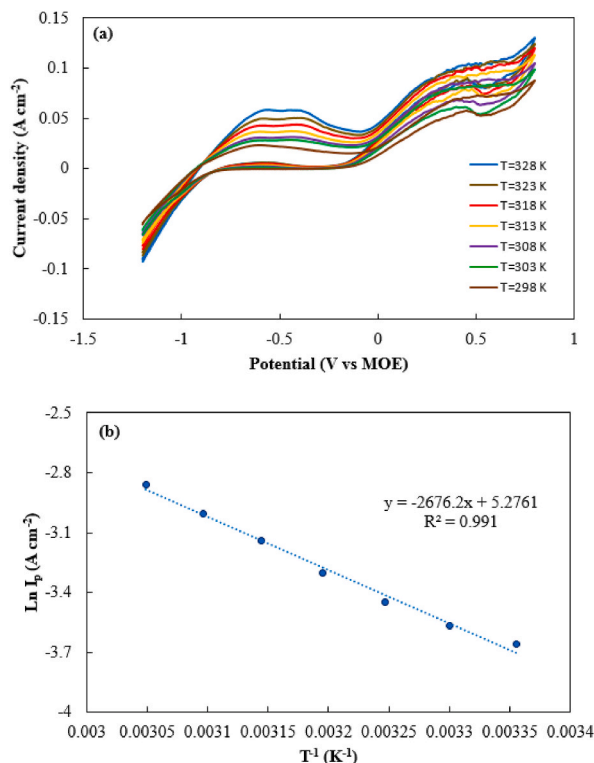
Fig. 10. (a) CV curves of Ru_1–Ni_3/rGO/NF for different temperatures in NaOH 1 M + N_2H_4 0.04 M, (b) relation of Ln i_p vs. T^{-1}.
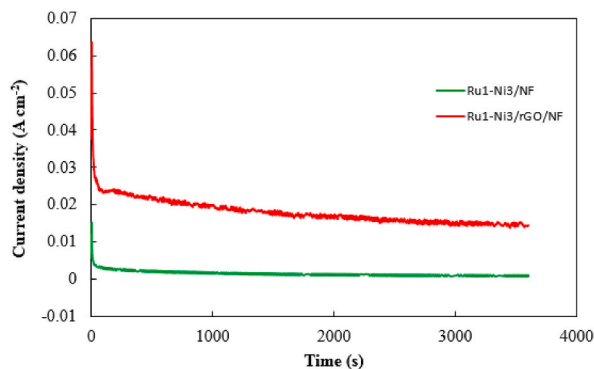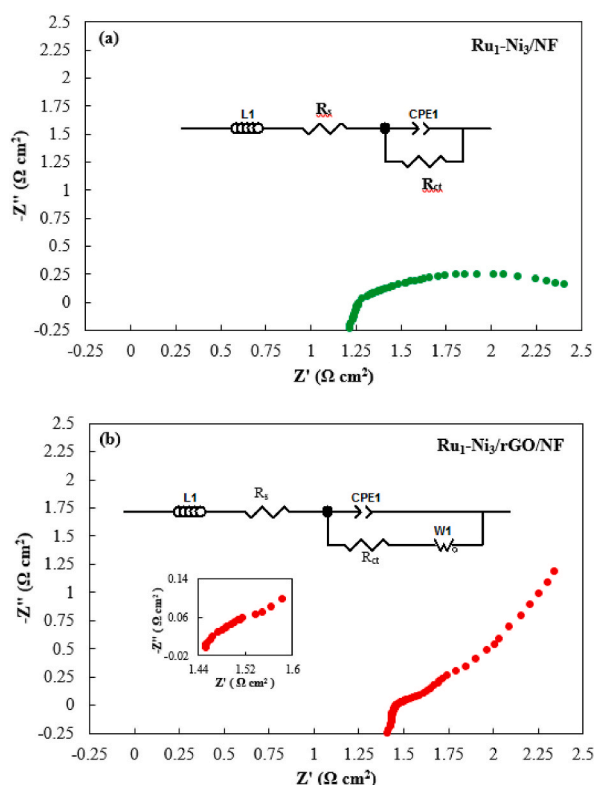

Fig. 11. CA curves of Ru_1–Ni_3/NF and Ru_1–Ni_3/GO/NF in NaOH 1 M + N_2H_4 0.04 M at −0.6 (V vs. MOE).

fuel cells (DHzHPFC) was investigated. The anolyte and catholyte solutions were (N_2H_4 x M + NaOH 2 M) and (H_2O_2 x M + H_2SO_4 0.5 M), respectively. The results related to different concentrations of fuel (N_2H_4) and oxidant (H_2O_2) were demonstrated in Table 2.

Fig. 13 (a, b) shows the I–P and I–V curves of DHzHPFC. According to the Nernst equation (Eq. (12)), the open circuit potential (OCP) and as a result, the power densities were increased with the addition of N_2H_4 and H_2O_2 concentrations (Fig. 13a and b), but for higher concentrations of N_2H_4 (2 M) and H_2O_2 (3 M) the power densities were decreased.

$$E = E^\circ + \frac{RT}{nF} \ln \frac{[N_2H_4][H_2O_2]^2}{[N_2][H_2O]^4} \tag{12}$$

This can relate to the chemical decomposition of H_2O_2, hydrolysis N_2H_4 and their crossover from the membrane. In addition, the power densities were decreased due to the poisoning of the electrode surface by gas bubbles generated by H_2O_2 decomposition and N_2H_4 hydrolysis [46–50]. The role of temperature is significant in electrochemical reactions. Therefore, the effect of temperature on the performance of DHzHPFC was studied and the results were shown in Fig. 13c. With the rise of temperature from 35 °C to 55 °C, the power density was increased. The high values of OCP and maximum power density show that the kinetics of H_2O_2 reduction and N_2H_4

Fig. 12. EIS curves (a) Ru_1–Ni_3/NF and (b) Ru_1–Ni_3/rGO/NF/NF in NaOH 1 M + N_2H_4 0.1 M and at −0.250 (V vs. MOE).

Table 1
Equivalent circuit parameters of Ru_1–Ni_3/rGO/NF and Ru_1–Ni_3/NF catalysts in NaOH 1 M + N_2H_4 0.1 M.

Electrode	Potential (mV vs MOE)	R_s (Ω cm^2)	R_{ct} (Ω cm^2)
Ru_1–Ni_3/rGO/NF	−250	1.5	0.1
Ru_1–Ni_3/NF	−250	1.2	1.4

Table 2
Power density of the direct N_2H_4–H_2O_2 single fuel cell with the anode electrode: Ru_1Ni_3/rGO/NF, and the cathode electrode Pt/C under different conditions.

$[N_2H_4]$/(mol L^{-1})	$[H_2O_2]$/(mol L^{-1})	Temperature/(°C)	Power density/(mW cm^{-2}) Accuracy $\pm$ 2
1	0.5	25	82
1	3	25	118
0.5	2	25	79
2	2	25	79
1	2	25	83
1	2	35	141
1	2	45	189
1	2	55	206

oxidation were enhanced with increasing the temperature [51]. The maximum power density was obtained 206 mW cm^{-2} which was related to (N_2H_4 1 M + NaOH 2 M) as the anolyte and (H_2O_2 2 M + H_2SO_4 0.5 M) as the catholyte solutions in 328 K.

A stability test was performed for a single cell with the Ru_1–Ni_3/rGO/NF as an anode and the Pt/C as a cathode, (N_2H_4 1 M + NaOH 2 M) as an anolyte and (H_2O_2 2 M + H_2SO_4 0.5 M) in the role of a catholyte at a constant current of 50 mA cm^{-2} (Fig. 13d). The potential decay from the initial value by applying discharging current of 50 mA cm^{-2} to DHzHPFC. After a few seconds, the cell potential became stable and this stability continued until the end of the test. The subsequent oscillations in the cell potential were related to the addition of a new fuel solution, change in cell temperature, produced H_2 from the anode due to N_2H_4 hydrolysis and produced O_2 from the cathode due to H_2O_2 decomposition. These gas bubbles were collected on the electrode and blocked active sites. As a result, it decreased the performance of the cell. As shown in Fig. 13d, the Ru_1–Ni_3/rGO/NF in the role of an anode and the Pt/C in
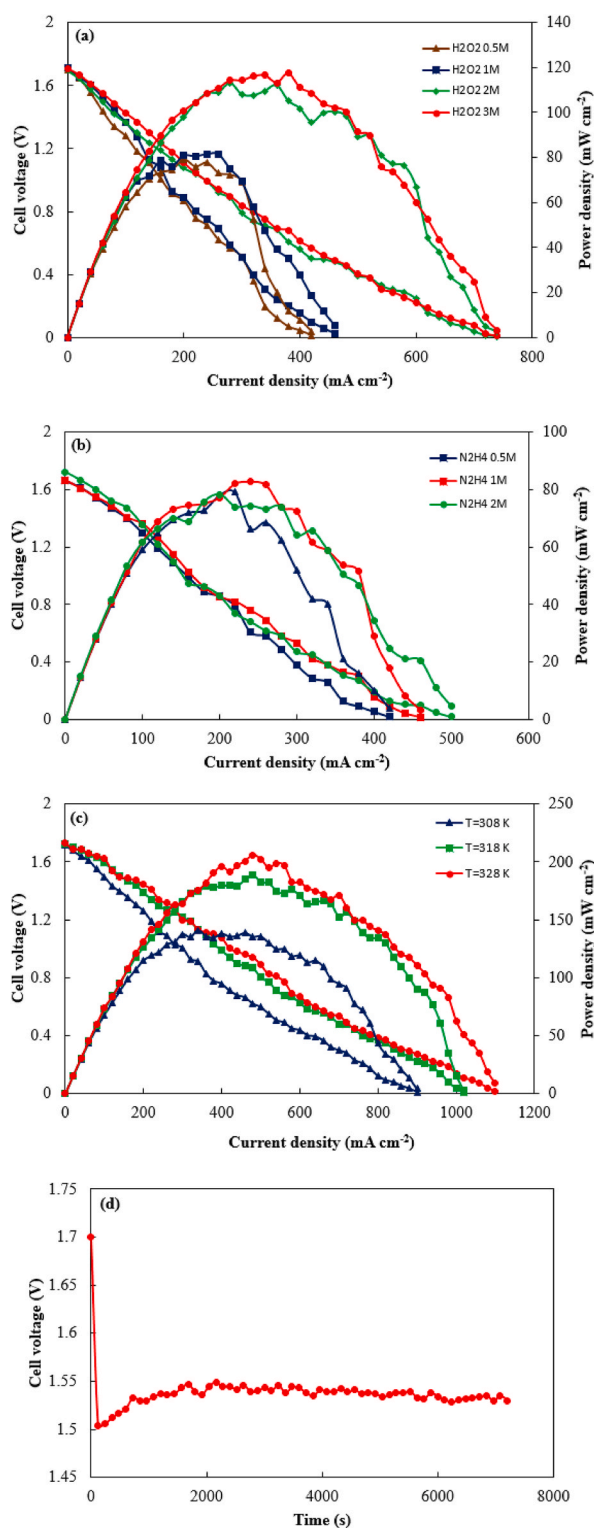
Fig. 13. I–P and I–V curves of Ru_1–Ni_3/rGO/NF for different concentrations of (a) H_2O_2 (b) N_2H_4 (c) different temperatures (d) stability test at a discharging current of 50 mA cm^{-2}.

Table 3

Comparison of power density values obtained for DHzHPFC by various electrocatalysts.

Anode	Cathode	Membrane	Anolyte	Catholyte	T (°C)	[a]Power density (mW cm^{-2})	Ref.
Ni foam@Ag–Ni	Pd/CFC	Nafion 115	KOH 1 M + N$_2$H$_4$ 0.045 M	H$_2$O$_2$ 1 M + H$_2$SO$_4$ 2 M	–	7	[52]
Pt$_{53}$Cu$_{47}$/C (0.5 mg cm^{-2})	Pt/C (20 wt%) (1.0 mg cm^{-2})	Tokuyama	KOH 1.0 M + N$_2$H$_4$ 1.0 M	O$_2$ flow rate: 30 SCCM	80	56	[53]
Ni0.6Co0.4 nanosheets (1.4 mg cm^{-2})	Pt/C (40.0 wt%)	Nafion 115	KOH 4.0 M + N$_2$H$_4$ 20.0 wt%	H$_2$O$_2$ 20.0% + H$_2$SO$_4$ 0.5 M	80	107	[54]
Pd/CNT (1.0 mg cm^{-2})	Pt/C (0.25 mg cm^{-2})	Nafion 117	NaOH 1.0 M + N$_2$H$_4$ 2.0 M	O$_2$ flow rate: 150.0 mL min^{-1}	60	110	[55]
Co–Au/C (1.0 mg cm^{-2})	Au/C (1.0 mg cm^{-2})	Nafion 117	NaOH 2.0 M + N$_2$H$_4$ 2.0 M	H$_2$O$_2$ 2.0 M + H$_2$SO$_4$ 0.5 M	60	123	[56]
MoCx–NC (1.0 mg cm^{-2})	Pt/C (1.0 mg cm^{-2})	KOH-doped PBI	KOH 6.0 M + N$_2$H$_4$ 0.5 M	O$_2$ Flux: 0.2 slpm	80	158	[57]
Ni@Pd/rGO (1.0 mg cm^{-2})	Pt/C (0.5 mg cm^{-2})	Nafion 117	NaOH 2.0 M + N$_2$H$_4$ 1.0 M	H$_2$O$_2$ 2.0 M + H$_2$SO$_4$ 0.5 M	60	205	[58]
Ni@Ru/rGO (1.0 mg cm^{-2})	Pt/C (0.5 mg cm^{-2})	Nafion 117	NaOH 2.0 M + N$_2$H$_4$ 1.0 M	H$_2$O$_2$ 2.0 M + H$_2$SO$_4$ 0.5 M	60	139	[58]
Pd–Ni/N-rGO (1.0 mg cm^{-2})	Pt/C (0.5 mg cm^{-2})	Nafion 117	NaOH 2.0 M + N$_2$H$_4$ 1.0 M	H$_2$O$_2$ 2.0 M + H$_2$SO$_4$ 0.5 M	60	217	[9]
Free binder Anode: Ru$_1$–Ni$_3$/rGO/NF	Pt/C (0.5 mg cm^{-2})	Nafion 117	NaOH 2.0 M + N$_2$H$_4$ 1.0 M	H$_2$O$_2$ 2.0 M + H$_2$SO$_4$ 0.5 M	55	206	This work

[a] The numbers related to the power density are reported in the table with approximations. To know the exact power density refer to the relevant reference.

the role of a cathode in DHzHPFC display relatively stable performance after the first few seconds. Finally, the performance of DHzHPFC for anode and cathode electrocatalysts has been compared in different literature and presented in Table 3. According to Table 3, the Ru$_1$–Ni$_3$/rGO/NF electrocatalyst in the role of anode and the Pt/C electrocatalyst in the role of cathode displayed an equal or greater catalytic performance.

4. Conclusion

The Ru$_1$–Ni$_3$/rGO/NF catalyst was synthesized by the combination of electroreduction and electroplating methods and then used as the free-binder anode electrocatalyst for HzOR. The morphology and surface analysis of the synthesized Ru$_1$–Ni$_3$/rGO/NF catalyst were investigated by FE-SEM, XRD, FT-IR, and Raman spectroscopy. The results confirmed the successful synthesis of Ru$_1$–Ni$_3$/rGO/NF. This electrocatalyst showed the highest EASA (677.5 cm^2) in comparison to other electrodes. From the electrochemical results including CV, EIS, and CA, it is clear that the Ru$_1$–Ni$_3$/rGO/NF electrocatalyst has good electrocatalytic activity and stability and can be a good promising candidate for HzOR. The activation energy for hydrazine oxidation on the Ru$_1$–Ni$_3$/rGO/NF electrocatalyst was 22.24 kJ mol^{-1}. In addition, the HzOR on Ru$_1$–Ni$_3$/rGO/NF electrocatalyst is irreversible and controlled by a diffusion process. Besides, EIS outcomes show that, in the range of hydrazine oxidation activation (-0.250 V vs. MOE), the Ru$_1$–Ni$_3$/rGO/NF electrocatalyst has low electrochemical charge transfers resistance (R$_{ct}$ = 0.1 Ω cm^2), that it is significantly less than charge transfers resistance of the Ru$_1$–Ni$_3$/NF electrocatalyst (R$_{ct}$ = 1.4 Ω cm^2). Therefore, the rGO has increased the electrocatalytic properties due to its high electrical conductivity and the structure with a large specific surface area. Fuel cell performance tests show that the synthesized Ru$_1$–Ni$_3$/rGO/NF electrocatalyst is a promising anodic catalyst for DHzHPFCs with a power density of 206 mWcm^{-2}, and excellent stability. These results prove that the Ru$_1$–Ni$_3$/rGO/NF free-binder anode is a promising candidate for usage as the electrocatalyst in the future application of DHzHPFCs because of its excellent structural stability, ease of synthesis, low cost, and high catalytic performance.

Author contribution statement

Mir ghasem Hosseini: Conceived and designed the experiments; Analyzed and interpreted the data.
Tahereh Mohammadi: Performed the experiments; Analyzed and interpreted the data; Wrote the paper.
Karim Asadpour-Zeynali: Contributed reagents, materials, analysis tools or data.
Mir Reza Majidi: Contributed reagents, materials, analysis tools or data; Wrote the paper.

Data availability statement

Data will be made available on request.

Declaration of competing interest

The authors declare that they have no known competing financial interests or personal relationships that could have appeared to

influence the work reported in this paper.

Acknowledgments

References

[1] S. Khan, et al., Ruthenium and palladium oxide promoted zinc oxide nanoparticles: efficient electrocatalysts for hydrazine oxidation reaction, J. Electroanal. Chem. 917 (2022), 116422.

[2] S. Song, et al., Oxygen-doped MoS_2 nanoflowers with sulfur vacancies as electrocatalyst for efficient hydrazine oxidation, J. Electroanal. Chem. 906 (2022), 115986.

[3] S. Kottarathil, et al., Selective borohydride oxidation reactions of zeolitic imidazolate framework-derived bimetallic carbon alloy electrocatalysts for alkaline fuel cell applications, ACS Appl. Energy Mater. 5 (10) (2022) 12571–12582.

[4] C. Song, et al., A novel electrode of ternary CuNiPd nanoneedles decorated Ni foam and its catalytic activity toward NaBH4 electrooxidation, Electrochim. Acta 299 (2019) 395–404.

[5] J. Yu, et al., Defect-rich walnut-like copper-doped $Ni(PO_3)_2$ catalyst towards ammonia borane electrooxidation reaction with high performance, J. Mater. Chem. 10 (4) (2022) 2035–2044.

[6] N. Firdous, N.K. Janjua, $CoPtx/\gamma$-Al2O3 bimetallic nanoalloys as promising catalysts for hydrazine electrooxidation, Heliyon 5 (3) (2019), e01380.

[7] A. Serov, C. Kwak, Direct hydrazine fuel cells: a review, Appl. Catal. B Environ. 98 (1–2) (2010) 1–9.

[8] H. Wen, et al., In situ grown Ni phosphide nanowire array on Ni foam as a high-performance catalyst for hydrazine electrooxidation, Appl. Catal. B Environ. 241 (2019) 292–298.

[9] M.G. Hosseini, et al., Palladium-nickel electrocatalysts on nitrogen-doped reduced graphene oxide nanosheets for direct hydrazine/hydrogen peroxide fuel cells, Catalysts 11 (11) (2021) 1372.

[10] M.B. Askari, et al., Electro-oxidation of hydrazine on $NiFe_2O_4$-rGO as a high-performance nano-electrocatalyst in alkaline media, Mater. Chem. Phys. 275 (2022), 125313.

[11] K. Asazawa, et al., A platinum-free zero-carbon-emission easy fuelling direct hydrazine fuel cell for vehicles, Angew. Chem. 119 (42) (2007) 8170–8173.

[12] N.V. Rees, R.G. Compton, Carbon-free energy: a review of ammonia-and hydrazine-based electrochemical fuel cells, Energy Environ. Sci. 4 (4) (2011) 1255–1260.

[13] L.Q. Ye, et al., Hydrazine electrooxidation on a composite catalyst consisting of nickel and palladium, J. Power Sources 196 (3) (2011) 956–961.

[14] W.X. Yin, et al., Effects of NaOH addition on performance of the direct hydrazine fuel cell, J. Power Sources 182 (2) (2008) 520–523.

[15] J. Li, et al., Polyethyleneimine decorated graphene oxide-supported $Ni_{1-x}Fe_x$ bimetallic nanoparticles as efficient and robust electrocatalysts for hydrazine fuel cells, Catal. Sci. Technol. 3 (12) (2013) 3155–3162.

[16] J. Sanabria-Chinchilla, et al., Noble metal-free hydrazine fuel cell catalysts: EPOC effect in competing chemical and electrochemical reaction pathways, J. Am. Chem. Soc. 133 (14) (2011) 5425–5431.

[17] T. Sakamoto, et al., Operando XAFS study of carbon supported Ni, NiZn, and Co catalysts for hydrazine electrooxidation for use in anion exchange membrane fuel cells, Electrochim. Acta 163 (2015) 116–122.

[18] X. Liu, et al., Ni_3S_2@Ni foam 3D electrode prepared via chemical corrosion by sodium sulfide and using in hydrazine electro-oxidation, Electrochim. Acta 213 (2016) 730–739.

[19] S. Lu, et al., Study of carbon black supported amorphous Ni–B nano-catalyst for hydrazine electrooxidation in alkaline media, RSC Adv. 4 (51) (2014) 26940–26945.

[20] P. Yan, et al., Preparation of Au nanoparticles modified TiO_2/C core/shell nanowire array and its catalytic performance for NaBH4 oxidation, J. Electroanal. Chem. 745 (2015) 56–60.

[21] H. Gong, et al., Hydrothermal preparation of MoS_2 nanoflake arrays on Cu foil with enhanced supercapacitive property, Electrochim. Acta 227 (2017) 101–109.

[22] Z. Feng, et al., In situ grown nanosheet NiZn alloy on Ni foam for high performance hydrazine electrooxidation, Electrochim. Acta 304 (2019) 275–281.

[23] M.G. Hosseini, R. Mahmoodi, Improvement of energy conversion efficiency and power generation in direct borohydride-hydrogen peroxide fuel cell: the effect of Ni-M core-shell nanoparticles (M = Pt, Pd, Ru)/Multiwalled Carbon Nanotubes on the cell performance, J. Power Sources 370 (2017) 87–97.

[24] D. Zhang, et al., Three-dimensional functionalized graphene networks modified Ni foam based gold electrode for sodium borohydride electrooxidation, Int. J. Hydrogen Energy 41 (27) (2016) 11593–11598.

[25] F. Wang, et al., The preparation and performance of a novel spherical spider web-like structure RuNi/Ni foam catalyst for NaBH4 methanolysis, Int. J. Hydrogen Energy 44 (26) (2019) 13185–13194.

[26] X. Wu, et al., Functionalized three-dimensional graphene networks for high performance supercapacitors, Carbon 92 (2015) 26–30.

[27] H. Yan, et al., Electrochemical reduction approach-based 3D graphene/Ni (OH) 2 electrode for high-performance supercapacitors, Electrochim. Acta 154 (2015) 9–16.

[28] D. Zhang, et al., Nickel particles supported on multi-walled carbon nanotubes modified sponge for sodium borohydride electrooxidation, Electrochem. Commun. 35 (2013) 128–130.

[29] D. Zhang, et al., N_2H_4 electrooxidation at negative potential on novel wearable nano-Ni-MWNTs-textile electrode, Mater. Sci. Eng: B 188 (2014) 48–53.

[30] M. Chen, et al., One-step growth of reduced graphene oxide on arbitrary substrates, Carbon 144 (2019) 457–463.

[31] B. Li, et al., Reduced graphene oxide foam supported CoNi nanosheets as an efficient anode catalyst for direct borohydride hydrogen peroxide fuel cell, Appl. Surf. Sci. 491 (2019) 659–669.

[32] C. Wu, et al., In situ reduction of graphene oxide to improve the thermal and wettability properties of urea-melamine-modified phenol formaldehyde resin composites, Mater. Res. Express 6 (2) (2019), 025302.

[33] F. Guo, et al., Enhancement of direct urea-hydrogen peroxide fuel cell performance by three-dimensional porous nickel-cobalt anode, J. Power Sources 307 (2016) 697–704.

[34] S. Trasatti, O. Petrii, Real surface area measurements in electrochemistry, Pure Appl. Chem. 63 (5) (1991) 711–734.

[35] R.M. Penner, C.R. Martin, Preparation and electrochemical characterization of ultramicroelectrode ensembles, Anal. Chem. 59 (21) (1987) 2625–2630.

[36] M.W. Louie, A.T. Bell, An investigation of thin-film Ni–Fe oxide catalysts for the electrochemical evolution of oxygen, J. Am. Chem. Soc. 135 (33) (2013) 12329–12337.

[37] B.S. Yeo, A.T. Bell, In situ Raman study of nickel oxide and gold-supported nickel oxide catalysts for the electrochemical evolution of oxygen, J. Phys. Chem. C 116 (15) (2012) 8394–8400.

[38] H. Wang, et al., Three-dimensional petal-like graphene Co3. 0Cu1. 0 metal organic framework for oxygen evolution reaction, J. Alloys Compd. 884 (2021), 161144.

[39] X. Li, et al., MOF derived Co3O4 nanoparticles embedded in N-doped mesoporous carbon layer/MWCNT hybrids: extraordinary bi-functional electrocatalysts for OER and ORR, J. Mater. Chem. 3 (33) (2015) 17392–17402.

[40] B. Li, et al., Effect of graphene on the performance of nickel foam-based CoNi nanosheet anode catalyzed direct urea-hydrogen peroxide fuel cell, Int. J. Hydrogen Energy 45 (17) (2020) 10569–10579.

[41] P. He, et al., Reverse micelle synthesis of AuNi alloy as electrocatalyst of borohydride oxidation, Int. J. Hydrogen Energy 37 (2) (2012) 1254–1262.

[42] T. Vats, et al., Facile synthesis of pristine graphene-palladium nanocomposites with extraordinary catalytic activities using swollen liquid crystals, Sci. reports 6 (1) (2016) 1–11.

[43] D.M.F. Santos, C.A.C. Sequeira, Cyclic voltammetry investigation of borohydride oxidation at a gold electrode, Electrochim. Acta 55 (22) (2010) 6775–6781.

[44] A.J. Bard, L.R. Faulkner, H.S. White, Electrochemical Methods: Fundamentals and Applications, 2022 (John Wiley & Sons).

[45] M.G. Hosseini, M. Momeni, M. Faraji, Highly active nickel nanoparticles supported on TiO_2 nanotube electrodes for methanol electrooxidation, Electroanalysis 22 (22) (2010) 2620–2625.

[46] M. Abdolmaleki, I. Ahadzadeh, H. Goudarziafshar, Direct hydrazine-hydrogen peroxide fuel cell using carbon supported Co@ Au core-shell nanocatalyst, Int. J. Hydrogen Energy 42 (23) (2017) 15623–15631.

[47] D. Cao, et al., An alkaline direct $NaBH_4$–H_2O_2 fuel cell with high power density, J. Power Sources 190 (2) (2009) 346–350.

[48] W. Haijun, et al., Influence of operation conditions on direct $NaBH_4/H_2O_2$ fuel cell performance, Int. J. Hydrogen Energy 35 (7) (2010) 2648–2651.

[49] B. Liu, et al., Performance improvement of a micro borohydride fuel cell operating at ambient conditions, Electrochim. Acta 50 (18) (2005) 3719–3725.

[50] N. Duteanu, et al., A parametric study of a platinum ruthenium anode in a direct borohydride fuel cell, J. Appl. Electrochem. 37 (9) (2007) 1085–1091.

[51] J. Ma, Y. Sahai, R.G. Buchheit, Direct borohydride fuel cell using Ni-based composite anodes, J. Power Sources 195 (15) (2010) 4709–4713.

[52] Y. Lei, et al., Facile fabrication of hierarchically porous Ni foam@ Ag-Ni catalyst for efficient hydrazine oxidation in alkaline medium, J. Taiwan Inst. Chem. Eng. 105 (2019) 75–84.

[53] R. Crisafulli, et al., On the promotional effect of Cu on Pt for hydrazine electrooxidation in alkaline medium, Appl. Catal. B Environ. 236 (2018) 36–44.

[54] G. Feng, et al., Single crystalline ultrathin nickel–cobalt alloy nanosheets array for direct hydrazine fuel cells, Adv. Sci. 4 (3) (2017), 1600179.

[55] V.A. Paganin, E.A. Ticianelli, E.R. Gonzalez, Development and electrochemical studies of gas diffusion electrodes for polymer electrolyte fuel cells, J. Appl. Electrochem. 26 (3) (1996) 297–304.

[56] M. Abdolmaleki, I. Ahadzadeh, H. Goudarziafshar, Direct hydrazine-hydrogen peroxide fuel cell using carbon supported Co@Au core-shell nanocatalyst, Int. J. Hydrogen Energy 42 (23) (2017) 15623–15631.

[57] J. Deng, et al., Molybdenum carbide-nitrogen doped carbon composites as effective non-precious electrocatalyst for direct hydrazine fuel cell, Electrochim. Acta 384 (2021), 138417.

[58] M.G. Hosseini, R. Mahmoodi, M. Abdolmaleki, High performance direct hydrazine–hydrogen peroxide fuel cell using reduced graphene oxide supported Ni@ M (M= Pt, Pd, Ru) nanoparticles as novel anodic electrocatalysts, New J. Chem. 42 (14) (2018) 12222–12233.